Accelerated Computation of the Physical Optics Approximation for Near-Field Single- and Double-Bounces Backscattering

Christophe Bourlier [iD], Gildas Kubické, and Philippe Pouliguen

Abstract— This article deals with the acceleration of the physical optics (PO) approximation for the backscattering computation in the near and far fields, for both single-bounce (SB) and double-bounce (DB) PO contributions. It is based on physical arguments, which allow us to apply either a closed-form expression (rapid calculation) or a numerical double integration to evaluate the scattered field from subsurfaces of a given mesh. The use of the closed-form expression is governed by two criteria, which must be extended to the bistatic case and also to the DB: the conventional Fraunhofer (related to the far-field zone) criterion and the chord error (related to the surface curvature) criterion. The proposed method is tested on a dihedral geometry.

Index Terms— Fast algorithm, high-frequency methods, physical optics (PO), radar cross section (RCS).

NOMENCLATURE

DB   Double bounce.
IPO   Iterative physical optics.
PO   Physical optics.
PO1   PO at the first order (contribution of the SB).
PO2   PO at the second order (contribution of the DB).
RCS   Radar cross section.
SB   Single bounce.
SC   Scattering coefficient.
SD   Subsurface decomposition.

I. INTRODUCTION

IN THE low- and intermediate-frequency regimes, exact numerical methods, such as the method of moments (MoM) [1], can be used for solving the problem of scattering from a target. At very high frequencies, such methods become unattractive due to their high computational complexity. Fortunately, for such frequencies, asymptotic techniques, such as the ray-based [2] and PO-based methods,

become applicable for structures with radii of curvature large compared to the wavelength. The ray methods provide a phenomenological solution, cast in terms of reflected and diffracted ray contributions, but suffer from high sensitivity to geometrical details and occasional failures.

Using the PO approximation for general (nonconvex) geometries, in order to capture the relevant scattering mechanisms, one may describe the solution as a series of contributions, each generated by its respective term in a series of source distributions on the scatterer's surface, named "bounces." The first term in the series, the "SB" contribution, provides a sufficient description of the scattering mechanism, asymptotically associated with the specular reflection, which can be significant for convex geometries. For concave geometries, accurate computation of the scattered field requires, in addition, to take into account at least the second-order term in the series, the "double-bounce" contribution, which asymptotically corresponds to two reflections on surfaces of the scatterer. For particular geometries, like a dihedral, the DB scattering can become the main contribution.

For some applications, the target can be close to the transmitter/receiver and then the Fraunhofer criterion is not satisfied, which means that the scattered field must be computed in the near field. The computation of the multi-bounce contributions involves multiple surface integrations. For instance, for the calculation of the SB contribution, twofold integrations are required, whereas for the DB contribution, fourfold integrations are required. These integrations dominate the computational complexity of the entire PO solution and become a computational bottleneck for large scatterers.

For canonical geometries, the calculation of the SB integral can be analytically done [3]–[8] by introducing special functions, especially in the near field and for complex shapes. For complex geometries, numerical techniques have also been developed [9]–[15] to evaluate the SB integral, especially for different excitations [11], [12] (see also [16] for a complete review of this method). For the calculation of the DB integral, it is impossible to derive closed-form expressions even for canonical geometries, without the introduction of simplifying assumptions [17]–[22] (like the geometric optics approximation or by expanding the kernel into a Taylor series expansion). For any geometry, to overcome this issue, the multilevel PO (MLPO) [16] has been developed both in the near and far fields, for which the time saving is mainly obtained from

the treatment of multiple source positions/angles/frequencies. Other accelerations of PO were proposed in the context of open-ended cavities with the IPO method [23]–[28].

This article addresses the general issue of the acceleration of the calculation of the SB and DB contributions, both in the near and far fields, in the backscattering direction by developing the SD PO "PO + SD" method. It consists in applying either a closed-form expression (rapid calculation) or a numerical double integration to evaluate the scattered field from subsurfaces of a given mesh. This idea has been tested in [10]. The starting point of this algorithm is similar to that of MLPO, which also decomposes the structure into subsurfaces, but it is different for the calculations of the fields scattered by the subsurfaces. To apply the closed-form expression, two criteria must be satisfied. The first one corresponds to the Fraunhofer criterion, which gives the distance r_0, from which, both the transmitter (which can be a subsurface) and the receiver (which can be a subsurface) can be considered to be in the far field. For the monostatic case, this distance is often defined by $r_0 \geq 4d^2/\lambda_0$, in which d is the largest dimension of the subsurface and λ_0, the electromagnetic wavelength. In this paper, the distance r_0 is derived rigorously for the bistatic case and extended to the monostatic case for the DB. The second criterion is related to the curvature of the subsurface. The use of a closed-form expression of the scattered field, without introducing special functions, implies that the curvature of the subsurface can be neglected. This leads to the derivation of the "chord error" criterion for the bistatic case and its extension to the monostatic case for the DB.

This paper is organized as follows. Using the PO method, Section II derives the bistatic SC (the RCS is obtained from the SC by taking its square modulus) for the SB and DB and simplifies them for the monostatic case. In Section III, method "PO + SD" is presented, in which the two criteria are derived for the SB and DB and the resulting monostatic SC is derived. Section IV presents the numerical results of the monostatic SC and the time saving. Section V gives concluding remarks.

The time convention $e^{-j\omega t}$ is used throughout this paper.

II. SCATTERING COEFFICIENT COMPUTED BY THE PHYSICAL OPTICS IN THE NEAR FIELD

A. Bistatic Case

In the near field, Pouliguen et al. [3] showed that the PO-scattered magnetic field of the SB is expressed as (for a perfectly conducting scatterer)

$$H_s = -\frac{j}{\lambda_0} \iint_{S_I} G(r_s)[\hat{n} \wedge H_i] \wedge \hat{r}_s \frac{e^{jk_0 r_s}}{r_s} dS \quad (1)$$

where

$$G(r) = 1 + \frac{j}{k_0 r}. \quad (2)$$

Here, the following can be defined (see Fig. 1).

1) λ_0 ($k_0 = 2\pi/\lambda_0$) is the electromagnetic wavelength in free space.
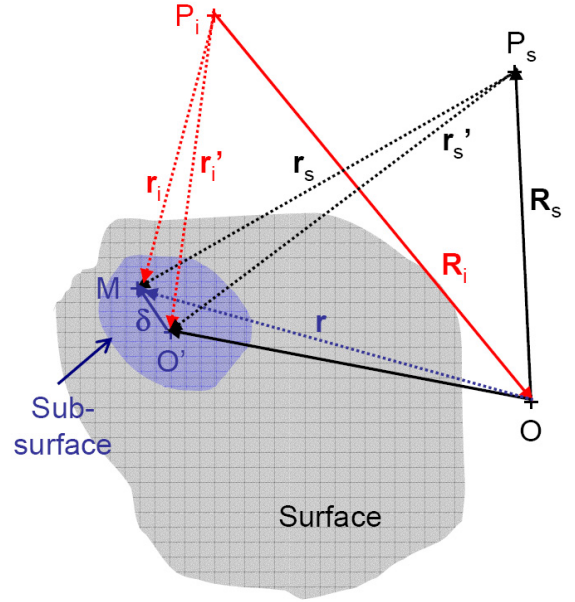2) $r_s = r - R_s$, where $-r_s$ is the observation point defined from the point M on the surface of the scatterer.
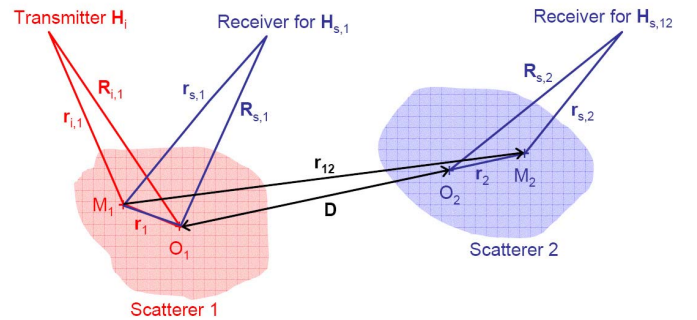

Fig. 1. Geometry for the SB case (PO1).

Fig. 2. Geometry to calculate the scattered field from PO2 (DB).

3) The vector $R_s = (x_s, y_s, z_s)$ stands for the location of the receiver.
4) $\hat{n} = \hat{n}(r)$ is the normal to the surface S at the point M of coordinates $r = (x, y, z)$.
5) $H_i = H_i(r)$ is the incident magnetic field on the surface.
6) S_I is the portion of the surface illuminated by the incident wave. The points of the surface are illuminated if $\hat{r}_i \cdot \hat{n} < 0$, where $\hat{r}_i$ stands for the direction of the incident wave.
7) The boldface stands for a vector and the hat ˆ indicates that the vector is unitary ($\hat{u} = u/\|u\|$).

As shown in Fig. 2, the scattered magnetic field at the second order of the DB, $H_{s,12}$, resulting from the scattering from scatterer 2 illuminated by scatterer 1, is obtained from (1), in which the incident magnetic field H_i is substituted for $H_{s,1}$, the magnetic field scattered by object 1. This leads to

$$H_{s,12} = -\frac{1}{\lambda_0^2} \iiiint_{S_{I1}, S_{I2}} \frac{G(r_{12})G(r_{s,2})e^{jk_0(r_{12}+r_{s,2})}}{r_{12} r_{s,2}}$$
$$\times \hat{n}_2 \wedge [(\hat{n}_1 \wedge H_{i,1}) \wedge \hat{r}_{12}] \wedge \hat{r}_{s,2} dS_1 dS_2 \quad (3)$$

where $\hat{\boldsymbol{n}}_1 = \hat{\boldsymbol{n}}(\boldsymbol{r}_1)$, $\hat{\boldsymbol{n}}_2 = \hat{\boldsymbol{n}}(\boldsymbol{r}_2)$, $\boldsymbol{H}_{i,1} = \boldsymbol{H}_i(\boldsymbol{r}_1)$, $\boldsymbol{r}_{12} = \boldsymbol{r}_2 - \boldsymbol{r}_1$, and $\boldsymbol{r}_{s,2}$ the observation point on the surface defined from scatterer 2. The subscripts "1" and "2" are added to distinguish scatterers 1 and 2. The points of the surface S_2 are illuminated (corresponding to the surface S_{I2}) from S_1 if $\hat{\boldsymbol{r}}_{12} \cdot \hat{\boldsymbol{n}}_2 < 0$.

The incident magnetic field can be expressed as

$$\boldsymbol{H}_i(r) = \frac{V_i}{Z_0} \frac{e^{jk_0 r}}{r} \hat{\boldsymbol{p}}_i \tag{4}$$

where V_i is the voltage source, Z_0 the wave impedance in free space, and $\hat{\boldsymbol{p}}_i$ the polarization state of the transmitter, which can be either vertical ($\hat{\boldsymbol{v}}_i$) or horizontal ($\hat{\boldsymbol{h}}_i$).

In addition, in the near field, the bistatic SC (the RCS is obtained from the SC by taking its square modulus) can be defined as [3]

$$\rho_{p_i p_s} = 2\sqrt{\pi} R_i R_s Z_0 \frac{\boldsymbol{H}_s \cdot \hat{\boldsymbol{p}}_s}{V_i} \tag{5}$$

where $\{R_{i,s}\}$ are the distances from the transmitter and the receiver, respectively, to the origin O, and $\hat{\boldsymbol{p}}_s$ is the polarization state of the receiver, which can be either vertical ($\hat{\boldsymbol{v}}_s$) or horizontal ($\hat{\boldsymbol{h}}_s$). The vectors are defined by $\hat{\boldsymbol{h}}_{i,s} = \hat{\boldsymbol{r}}_{i,s} \wedge \hat{\boldsymbol{z}} / \|\hat{\boldsymbol{r}}_{i,s} \wedge \hat{\boldsymbol{z}}\|$, where $\hat{\boldsymbol{z}} = (0, 0, 1)$ and $\hat{\boldsymbol{v}}_{i,s} = \hat{\boldsymbol{h}}_{i,s} \wedge \hat{\boldsymbol{r}}_{i,s}$.

Then, the substitution of (4) and (1) into (5) leads to

$$\rho_{p_i p_s} = \frac{2\sqrt{\pi}}{j\lambda_0} \iint_{S_I} [(\hat{\boldsymbol{n}} \wedge \hat{\boldsymbol{p}}_i) \wedge \hat{\boldsymbol{r}}_s] \cdot \hat{\boldsymbol{p}}_s$$
$$\times \frac{G(r_s) R_i R_s}{r_i r_s} e^{jk_0(r_i + r_s)} dS \tag{6}$$

where $\boldsymbol{r}_i = \boldsymbol{r} - \boldsymbol{R}_i$, in which $\boldsymbol{R}_i = (x_i, y_i, z_i)$ stands for the location of the transmitter.

The bistatic SC of the DB is derived from the substitution of (4) and (3) into (5) (in which $\boldsymbol{H}_s = \boldsymbol{H}_{s,12}$, $\boldsymbol{R}_i = \boldsymbol{R}_{i,1}$, and $\boldsymbol{R}_s = \boldsymbol{R}_{s,2}$), leading to

$$\rho_{p_i p_s,12} = -\frac{2\sqrt{\pi}}{\lambda_0^2} \iiiint_{S_{1I}, S_{2I}} \frac{R_{i,1} R_{s,2} G(r_{12}) G(r_{s,2})}{r_{i,1} r_{12} r_{s,2}}$$
$$\times e^{jk_0(r_{i,1} + r_{12} + r_{s,2})}$$
$$\times \{\hat{\boldsymbol{n}}_2 \wedge [(\hat{\boldsymbol{n}}_1 \wedge \hat{\boldsymbol{p}}_{i,1}) \wedge \hat{\boldsymbol{r}}_{12}] \wedge \hat{\boldsymbol{r}}_{s,2}\} \cdot \hat{\boldsymbol{p}}_{s,2} dS_1 dS_2. \tag{7}$$

Equations (6) and (7) are valid if the following conditions are satisfied.

1) To apply the PO approximation, the radii of curvature of the two surfaces are much larger than the wavelength λ_0.
2) For the definition of the SC, the electromagnetic field radiated by the antenna has a spherical wave structure.
3) For the definition of the SC, the scattered electromagnetic wave field has a spherical wave structure, locally plane on the receiving antenna.

In the conclusion, the total SC up to the second order is obtained from four sub-SCs

$$\rho_{p_i p_s,\text{tot}} = \rho_{p_i p_s,1} + \rho_{p_i p_s,2} + \rho_{p_i p_s,12} + \rho_{p_i p_s,21} \tag{8}$$

where the following can be defined.

1) $\rho_{p_i p_s,1}$ stands for the SC of scatterer 1 assumed to be alone [obtained from (6) by adding subscript 1].

2) $\rho_{p_i p_s,2}$ stands for the SC of scatterer 2 assumed to be alone [obtained from (6) by adding subscript 2].
3) $\rho_{p_i p_s,12}$ stands for the SC of scatterer 2 illuminated by scatterer 1.
4) $\rho_{p_i p_s,21}$ stands for the SC of scatterer 1 illuminated by scatterer 2.

B. Monostatic Case

For a monostatic configuration, $\boldsymbol{r}_s = \boldsymbol{r}_i$, (6) leads to

$$\rho_{p_i p_s} = \frac{2\sqrt{\pi}}{j\lambda_0} \iint_{S_I} \frac{(\hat{\boldsymbol{r}}_i \cdot \hat{\boldsymbol{n}}) \hat{\boldsymbol{p}}_i G(r_i) e^{j2k_0 r_i} R_i^2}{r_i^2} dS \tag{9}$$

where $(\hat{\boldsymbol{n}} \wedge \hat{\boldsymbol{p}}_i) \wedge \hat{\boldsymbol{r}}_i = (\hat{\boldsymbol{r}}_i \cdot \hat{\boldsymbol{n}}) \hat{\boldsymbol{p}}_i - (\hat{\boldsymbol{r}}_i \cdot \hat{\boldsymbol{p}}_i) \hat{\boldsymbol{n}} = (\hat{\boldsymbol{r}}_i \cdot \hat{\boldsymbol{n}}) \hat{\boldsymbol{p}}_i$.

In addition, $(\boldsymbol{r}_{i,1}, \boldsymbol{r}_{s,2})$ involved in (7) becomes $(\boldsymbol{r}_{i,2}, \boldsymbol{r}_{s,1})$ for $\rho_{p_i p_s,21}$, in which $\boldsymbol{r}_{s,2} = \boldsymbol{r}_{i,2}$ and $\boldsymbol{r}_{s,1} = \boldsymbol{r}_{i,1}$. Then,

$$\rho_{p_i p_s,12} + \rho_{p_i p_s,21}$$
$$= -\frac{2\sqrt{\pi}}{\lambda_0^2} \iiiint_{S_{1I}, S_{2I}} dS_1 dS_2$$
$$\times \frac{R_{i,1} R_{i,2} G(r_{12}) G_{p_i p_s}}{r_{i,1} r_{12} r_{i,2}} e^{jk_0(r_{i,1} + r_{12} + r_{i,2})} \tag{10}$$

where

$$G_{p_i p_s}$$
$$= G(r_{i,2})\{\hat{\boldsymbol{n}}_2 \wedge [(\hat{\boldsymbol{n}}_1 \wedge \hat{\boldsymbol{p}}_{i,1}) \wedge \hat{\boldsymbol{r}}_{12}] \wedge \hat{\boldsymbol{r}}_{i,2}\} \cdot \hat{\boldsymbol{p}}_{i,2}$$
$$- G(r_{i,1})\{\hat{\boldsymbol{n}}_1 \wedge [(\hat{\boldsymbol{n}}_2 \wedge \hat{\boldsymbol{p}}_{i,2}) \wedge \hat{\boldsymbol{r}}_{12}] \wedge \hat{\boldsymbol{r}}_{i,1}\} \cdot \hat{\boldsymbol{p}}_{i,1}. \tag{11}$$

To accelerate the computations of integrals (9) and (10), the SD method is presented in Section III.

III. EVALUATION OF SUBSURFACES CONTRIBUTIONS

This method consists in applying either a closed-form expression (rapid calculation) or a numerical double integration (done from a conventional trapezoidal rule) to evaluate the scattered field from the subsurfaces $\{S_n\}$ of a given mesh. The closed-form expression is valid if both the bistatic Fraunhofer and chord error criteria are satisfied. They are derived thereafter for the SB and DB.

A. Bistatic Fraunhofer and Chord Error Criteria

From Fig. 1, one has $\boldsymbol{r}_i = \boldsymbol{r}'_i + \boldsymbol{\delta}$. If $\delta = \|\boldsymbol{\delta}\| \ll r'_i = \|\boldsymbol{r}'_i\|$, then a Taylor series expansion up to the second order over δ and around zero leads to

$$r_i \approx r'_i + \delta \cos \phi'_i + \frac{\delta^2}{2r'_i} \sin^2 \phi'_i \tag{12}$$

where $\phi'_i = \widehat{(\boldsymbol{\delta}, \boldsymbol{r}'_i)}$. The δ term is related to the local behavior of a plane wave, whereas δ^2 is related to the local behavior of a spherical wave. The Fraunhofer criterion is obtained from (12) by neglecting the δ^2 term. In other words, this approximation is satisfied if $\delta^2 \sin^2 \phi'_i/(2r'_i)$ does not exceed λ_0/n_0 (typically n_0 is an integer ranging from 8 to 16) where λ_0 is the radar wavelength. This leads, for $k_0(r_i + r_s)$, to

$$\frac{\delta^2}{2} \left(\frac{\sin^2 \phi'_i}{r'_i} + \frac{\sin^2 \phi'_s}{r'_s} \right) \leq \frac{\lambda_0}{n_0}. \tag{13}$$

The maximum value of δ, named Δ, equals

$$\Delta = \max \left(\sqrt{(x - x')^2 + (y - y')^2 + (z - z')^2} \right)$$

$$\approx \sqrt{d'^2 + d'^2 + d'^2(\gamma_x'^2 + \gamma_y'^2)}$$

$$\approx |d'|\sqrt{2 + \gamma_x'^2 + \gamma_y'^2} \tag{14}$$

where d' is the radius of the circle circumscribing the subsurface and $z' - z$ is expressed from (17). Then, the subsurface can be considered to be in the far field if

$$r_{is}' \geq \frac{n_0 \Delta^2}{4\lambda_0}, \quad \frac{1}{r_{is}'} = \frac{1}{2}\left(\frac{\sin^2 \phi_i'}{r_i'} + \frac{\sin^2 \phi_s'}{r_s'} \right). \tag{15}$$

In other words, condition (15) is satisfied if the arithmetic mean of the curvature radii weighted by $\sin^2 \phi_{i,s}'$ of the incident and scattered wave is smaller than $4\lambda_0/(n_0\Delta^2)$.

For a monostatic configuration, $r_s' = r_i'$ and $\phi_s' = \phi_i'$, which lead to $r_i' \geq n_0 \Delta^2 \sin^2 \phi_i'/(4\lambda_0)$. For $n_0 = 16$ and $\sin \phi_i' = 1$, the conventional Fraunhofer criterion (for RCS application) is retrieved, $r_i' \geq 4\Delta^2/\lambda_0 \approx 8\ d'^2/\lambda_0$.

If criterion (15) is satisfied, from (12), $r_i \approx r_i' + \delta \cos \phi_i'$ and

$$r_i \approx r_i' + (x - x')\hat{r}_{ix}' + (y - y')\hat{r}_{iy}' + (z - z')\hat{r}_{iz}' \tag{16}$$

where $\boldsymbol{r}_i' = r_i'(\hat{r}_{ix}', \hat{r}_{iy}', \hat{r}_{iz}')$ and the point O' have coordinates (x', y', z').

To obtain a closed-form expression of the double integral over x and y, the term $z - z'$ is expanded as

$$z - z' \approx (x - x')\gamma_x' + (y - y')\gamma_y' \tag{17}$$

where $\gamma_x' = \partial z/\partial x|_{x=x',y=y'}$ and $\gamma_y' = \partial z/\partial y|_{x=x',y=y'}$. Using the same way as for criterion (13), expansion (17) is valid if

$$|\hat{r}_{iz}' + \hat{r}_{sz}'|F_{is}' < \frac{\lambda_0}{n_0} \tag{18}$$

where

$$F_{is}' = \left| \frac{\gamma_{xx}'(x - x')^2}{2} + \frac{\gamma_{yy}'(y - y')^2}{2} + \gamma_{xy}'(x - x')(y - y') \right| \tag{19}$$

and $\gamma_{xx}' = \partial^2 z/\partial x^2|_{x=x',y=y'}$, $\gamma_{yy}' = \partial^2 z/\partial y^2|_{x=x',y=y'}$ and $\gamma_{xy}' = \partial^2 z/\partial x \partial y|_{x=x',y=y'}$.

Introducing d', (18) becomes

$$|\hat{r}_{iz}' + \hat{r}_{sz}'|d'^2 \left| \frac{\gamma_{xx}'}{2} + \frac{\gamma_{yy}'}{2} + \gamma_{xy}' \right| < \frac{\lambda_0}{n_0}. \tag{20}$$

Criterion (20) is commonly named the "chord error" criterion.

In conclusion, if criteria (13) and (20) are satisfied, from (16) and (17), the distance $r_i + r_s - (r_i' + r_s') = \delta_{is}'$ is approximated by

$$\delta_{is}' = (x - x')\left[\hat{r}_{ix}' + \hat{r}_{sx}' + \gamma_x'(\hat{r}_{iz}' + \hat{r}_{sz}')\right]$$
$$+ (y - y')\left[\hat{r}_{iy}' + \hat{r}_{sy}' + \gamma_y'(\hat{r}_{iz}' + \hat{r}_{sz}')\right]. \tag{21}$$

B. Resulting Scattering Coefficient and Complexity of PO1

In (6), the kernel omitted of the phase term $e^{jk_0(r_i+r_s)}$ is approximated at the point $O'(x', y', z')$. Then, this term becomes independent of the integration variables x and y. This leads to

$$\rho_{p_i p_s} = \frac{2\sqrt{\pi}}{j\lambda_0} \sum_{n=1}^{N} \left[(\hat{\boldsymbol{n}}' \wedge \hat{\boldsymbol{p}}_i') \wedge \hat{\boldsymbol{r}}_s'\right] \cdot \hat{\boldsymbol{p}}_s' \frac{G(r_s')R_i R_s}{r_i' r_s'}$$

$$\times e^{jk_0(r_i' + r_s')} \iint_{S_I'} e^{jk_0\delta_{is}'} dS' \tag{22}$$

where the sum is done over all the subsurfaces, which satisfy criteria (13) and (20). The symbol prime indicates that the variables are constant for a given subsurface but depend on the subsurface n.

If the subsurface has a rectangular shape of lengths l_x' and l_y' with respect to the directions x and y, respectively, then

$$\iint_{S_I'} e^{jk_0\delta_{is}'} dS' = l_x' l_y' \mathrm{sinc}\left(\frac{a_x' l_x'}{2}\right) \mathrm{sinc}\left(\frac{a_y' l_y'}{2}\right) \tag{23}$$

where

$$\begin{cases} a_x' = \hat{r}_{ix}' + \hat{r}_{sx}' + \gamma_x'(\hat{r}_{iz}' + \hat{r}_{sz}') \\ a_y' = \hat{r}_{iy}' + \hat{r}_{sy}' + \gamma_y'(\hat{r}_{iz}' + \hat{r}_{sz}') \end{cases} \mathrm{sinc}(x) = \sin(x)/x. \tag{24}$$

The double integration is done analytically instead of numerically and the resulting complexity is $\mathcal{O}(M_x M_y)\eta^{\mathrm{PO1+SD}}$, where M_x and M_y are the numbers of the surface samples with respect to the x- and y-directions, respectively, and $\eta^{\mathrm{PO1+SD}} \in [0; 1]$ is defined as

$$\eta^{\mathrm{PO1+SD}} = \frac{1}{M_x M_y} \sum_{n=1}^{N} M_n \tag{25}$$

where

$$M_n = \begin{cases} 1, & \text{if (13) and (20) are satisfied} \\ \text{else}, & M_{x,n} M_{y,n} \end{cases} \tag{26}$$

where $M_{x,n}$ and $M_{y,n}$ are the numbers of the subsurface samples n with respect to the x- and y-directions, respectively. If all the subsurfaces do not satisfy the two criteria, then $\eta^{\mathrm{PO1+SD}} = (\sum_n M_{x,n}M_{y,n})/(M_x M_y) = 1$, corresponding to the complexity of the conventional PO1.

C. Resulting Scattering Coefficient and Complexity of PO2

In this section, the formulation is extended to the DB.

In (10), the distance $r_{i,1} + r_{12} + r_{i,2}$ can be approximated by

$$r_{i,1} + r_{12} + r_{i,2} \approx r_{i,1}' + r_{12}' + r_{i,2}' + \delta_1\left(\cos\phi_{i,1}' - \cos\phi_1'\right)$$
$$+ \delta_2\left(\cos\phi_{i,2}' + \cos\phi_2'\right) \tag{27}$$

where $\delta_1 = \|\overrightarrow{M_1' O_1'}\|$, $\delta_2 = \|\overrightarrow{M_2' O_2'}\|$, $\phi_{i,1}' = \widehat{(\delta_1, r_{i,1}')}$, $\phi_{i,2}' = \widehat{(\delta_2, r_{i,2}')}$, $\phi_1' = \widehat{(\delta_1, r_{12}')}$, and $\phi_2' = \widehat{(\delta_2, r_{12}')}$, in which $r_{12}' = \overrightarrow{O_2' O_1'}$ and $\{O_1', O_2'\}$ are the origins of the subsurfaces of scatterers 1 and 2, respectively. In addition, $r_{12}' = \|r_{12}'\|$, $r_{i,1}' = \|\overrightarrow{O_1' P_i}\|$, and $r_{i,2}' = \|\overrightarrow{O_2' P_i}\|$.

For the phase $k_0(r_{i,1} + r_{12} + r_{i,2})$, (27) is valid if

$$\frac{\Delta_1^2 \sin^2 \phi'_{i,1}}{2r'_{i,1}} + \frac{\Delta_2^2 \sin^2 \phi'_{i,2}}{2r'_{i,2}}$$

$$+ \frac{(\Delta_1 \sin \phi'_1 - \Delta_2 \sin \phi'_2)^2}{2r'_{12}} \leq \frac{\lambda_0}{n_0} \quad (28)$$

where $\Delta_p = |d'_i|\sqrt{2 + \gamma'^2_{p,x} + \gamma'^2_{p,y}}$. In addition, $\gamma'_{p,x} = \partial z_p/\partial x_p|_{x_p=x'_p, y_p=y'_p}$, $\gamma'_{p,y} = \partial z_p/\partial y_p|_{x_p=x'_p, y_p=y'_p}$, and d'_p is the radius of the circle circumscribing the prime subsurface of the scatterer $p = \{1, 2\}$. This corresponds to the monostatic Fraunhofer criterion extended to the DB.

Using the same approach as for PO1, from (27), the chord error criterion becomes

$$\left|(\hat{r}'_{iz,1} - \hat{r}'_{12z})d'^2_1 F'_1 + (\hat{r}'_{iz,2} + \hat{r}'_{12z})d'^2_2 F'_2\right| \leq \frac{\lambda_0}{n_0} \quad (29)$$

where

$$F'_p = \frac{\gamma'_{p,xx}}{2} + \frac{\gamma'_{p,yy}}{2} + \gamma'_{p,xy} \quad (30)$$

and $\gamma'_{p,xx} = \partial^2 z_p/\partial x_p^2|_{x_p=x'_p, y_p=y'_p}$, $\gamma'_{p,yy} = \partial^2 z_p/\partial y_p^2|_{x_p=x'_p, y_p=y'_p}$, and $\gamma'_{p,xy} = \partial^2 z_p/\partial x_p\partial y_p|_{x_p=x'_p, y_p=y'_p}$. In (29), the component $\hat{r}_z = \mathbf{r} \cdot \hat{z}/\|\mathbf{r}\|$.

In (10), the kernel omitted of the phase term equals $e^{jk_0(r_{i,1}+r_{12}+r_{i,2})}$ is approximated at the points $O'_1(x'_1, y'_1, z'_1)$ and $O'_2(x'_2, y'_2, z'_2)$. Then, this term becomes independent of the integration variables (x_1, y_1, x_2, y_2). This leads to

Equation (10)

$$= -\frac{2\sqrt{\pi}}{\lambda_0^2} \sum_{n_1=1}^{N_1} \sum_{n_2=1}^{N_2} \frac{R_{i,1} R_{i,2} G'_{p_i p_s} G(r'_{12})}{r'_{i,1} r'_{12} r'_{i,2} \lambda_0}$$

$$\times e^{jk_0(r'_{i,1}+r'_{12}+r'_{i,2})} \iiiint_{S'_{1I}, S'_{2I}} e^{jk_0\delta'_{12}} dS'_1 dS'_2 \quad (31)$$

where

$$\delta'_{12} = \sum_{p=1}^{p=2} (x_p - x'_p)a_{x,p} + (y_p - y'_p)a_{y,p} \quad (32)$$

in which

$$\begin{cases} a'_{x,1} = \hat{r}'_{ix,1} - \hat{r}'_{12x} + \gamma'_{x,1}(\hat{r}'_{iz,1} - \hat{r}'_{12z}) \\ a'_{y,1} = \hat{r}'_{iy,1} - \hat{r}'_{12y} + \gamma'_{y,1}(\hat{r}'_{iz,1} - \hat{r}'_{12z}) \\ a'_{x,2} = \hat{r}'_{ix,2} + \hat{r}'_{12x} + \gamma'_{x,2}(\hat{r}'_{iz,2} + \hat{r}'_{12z}) \\ a'_{y,2} = \hat{r}'_{iy,2} + \hat{r}'_{12y} + \gamma'_{y,2}(\hat{r}'_{iz,2} + \hat{r}'_{12z}) \end{cases} \quad (33)$$

where $\gamma'_{x,p} = \partial z_p/\partial x_p|_{x_p=x'_p, y_p=y'_p}$ and $\gamma'_{y,p} = \partial z_p/\partial y_p|_{x_p=x'_p, y_p=y'_p}$.

In (31), the sums are done over all the subsurfaces of the scatterers $p = \{1, 2\}$, which satisfy criteria (28) and (29). The symbol prime indicates that the variables are constant for a given subsurface but depend on the subsurfaces n_1 and n_2.

If the subsurface of the scatterer p has a rectangular shape of area $l'_{x,p} \times l'_{y,p}$, then the quadruple integrations can be analytically done, leading to

$$\prod_{p=1}^{p=2} l'_{x,p} l'_{y,p} \text{sinc}\left(\frac{a'_{x,p} l'_{x,p}}{2}\right) \text{sinc}\left(\frac{a'_{y,p} l'_{y,p}}{2}\right). \quad (34)$$

The resulting complexity is $\mathcal{O}(M_{x,1} M_{y,1} M_{x,2} M_{y,2}) \eta^{PO2+SD}$, where $M_{x,p}$ and $M_{y,p}$ are the numbers of samples on the surface p with respect to the x- and y-directions, respectively, and $\eta^{PO2+SD} \in [0; 1]$ is defined by

$$\eta^{PO2+SD} = \frac{1}{M_{x,1} M_{y,1} M_{x,2} M_{y,2}} \sum_{n_1=1}^{N_1} \sum_{n_2=1}^{N_2} M_{n_1,n_2} \quad (35)$$

where

$$M_{n_1,n_2} = \begin{cases} 1, & \text{if (28) and (29) are satisfied} \\ \text{else}, & M_{x,n_1} M_{y,n_1} M_{x,n_2} M_{y,n_2} \end{cases} \quad (36)$$

where M_{x,n_i} and M_{y,n_i} are the numbers of samples on the subsurface n_i of the scatterer i with respect to the directions x and y, respectively. If all the subsurfaces do not satisfy the two criteria, then $\sum_{n_1} \sum_{n_2} = M_{x,n_1} M_{y,n_1} M_{x,n_2} M_{y,n_2}$ and $\eta^{PO2+SD} = 1$, corresponding to the complexity of the conventional PO2.

For the DB and from (34), the integral is expressed as the product of two SB identical functions with different arguments related to subsurfaces of scatterers 1 and 2.

D. Numerical Implementation

The main steps of the algorithm are as follows.
1) Mesh the geometry.
2) Decompose the surface into subsurfaces of rectangular shapes. For a more general polygon shape (with the condition that two adjacent subsurfaces must remain connected), the formula of Gordon [30] can be applied.
3) One loop on the number of subsurfaces for PO1 and two loops on the number of subsurfaces of each scatterer.
4) Calculate the center coordinates and the circumscribed radii of the subsurfaces.
5) If the Fraunhofer and chord criteria are satisfied, then the integration is analytical, else numerical.
6) Cumulated sum of the resulting contribution.
7) Stop the loop(s).

IV. NUMERICAL RESULTS

A. Single Bounce

First, the monostatic SC of the SB is computed from PO1. The geometry is shown in Fig. 3: a corrugated surface defined as

$$z(x, y) = a \cos\left(\frac{2\pi x}{\Lambda_x}\right) \cos\left(\frac{2\pi y}{\Lambda_y}\right) \quad (37)$$

where a is the amplitude and $\{\Lambda_x, \Lambda_y\}$ the periods with respect to the x- and y-directions, respectively. The surface area is $L_x \times L_y$ and the wavelength equals $\lambda_0 = 3$ cm (the Radar frequency is $f = 10$ GHz).

In Fig. 3, $a = \lambda_0$, $L_x = L_y = 400\lambda_0$, $\Lambda_x = \Lambda_y = L_x/4 = 100\lambda_0$. The maximum values of the surface slopes are $\gamma_{x,\max} = \max(|\partial z/\partial x|) = 2\pi a/\Lambda_x = 0.0628$ ($a > 0$) and $\gamma_{y,\max} = \max(|\partial z/\partial y|) = 2\pi a/\Lambda_y = 0.0628$ with respect to the x- and y-directions, respectively. These values are chosen such as the multiple reflections on the surface can be neglected.
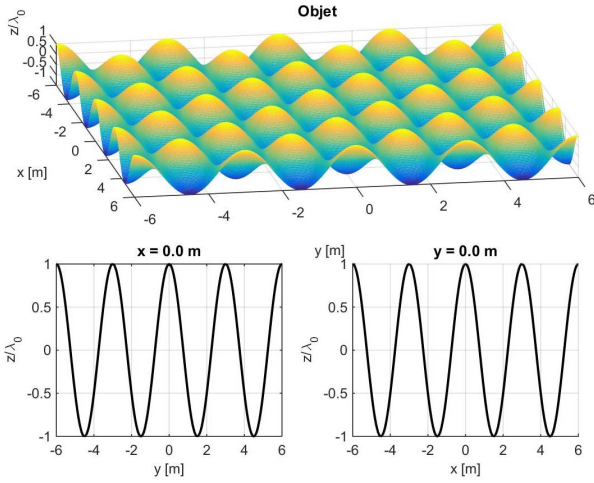
Fig. 3. Geometry for the computation of the monostatic SC of the SB. At the bottom, the full line is for $x = 0$ (left) and $y = 0$ (right). $a = \lambda_0 = 3$ cm, $L_x = L_y = 400\lambda_0$, and $\Lambda_x = \Lambda_y = L_x/4 = 100\lambda_0$.
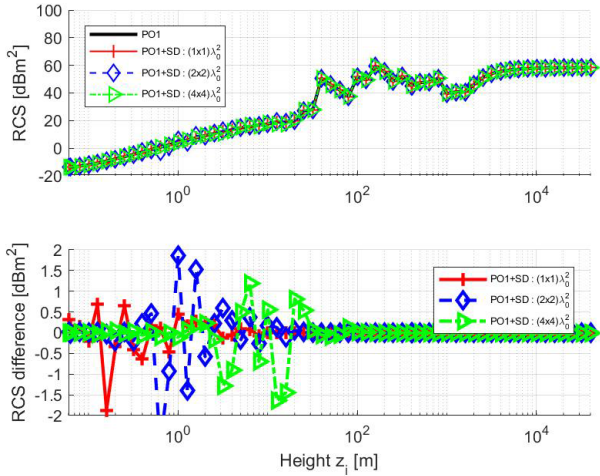

Fig. 4. Square modulus ρ^2 in dBm^2 scale of the monostatic SC computed from PO1 versus z_i (top). Difference in dB scale $|\rho^{PO1+SD}|^2$ (dB)–$|\rho^{PO1}|^2$ (dB) (against PO1 without acceleration) (bottom). $l'_x = l'_y = (1, 2, 4)\lambda_0$, $n_0 = 10$, and the surface is depicted in Fig. 3.

The sampling step with respect to the x- and y-directions, respectively, is $\Delta x = \Delta y = \lambda_0/10$ and $M_x = M_y = 4001$.

In addition, the positions of the receiver/transmitter are $x_i = y_i = 0$. z_i ranges from 0.06 to 40 000 m $> 4(L_x^2 + L_y^2)/\lambda_0 = 38\,400$ m, which is the conventional Fraunhofer distance.

At the top, Fig. 4 plots the square modulus $|\rho|^2$ of the monostatic SC versus z_i. In addition, at the bottom, to better see the differences, the ratio $|\rho^{PO1+SD}/\rho^{PO1}|^2$ is plotted in dB scale (becoming a difference). In the legend, the labels:

1) "PO1" means that the SC is computed from (9);
2) "PO1+SD ($l'_x \times l'_y$)" means that the SC is computed from (9) and (22) and $n_0 = 10$.

In addition, the lengths $l'_x = l'_y = \{1, 2, 4\}\lambda_0$ ($M_{x,n} = M_{y,n} = \{10, 20, 40\}$ $\forall p$ and $N = \{400^2, 200^2, 100^2\}$) are constant versus z_i. As z_i increases, the difference between SD + PO1 and PO1 decreases and does not exceed ± 2 dB.

Fig. 5 plots the computing time ratio t^{PO1}/t^{PO1+SD} versus z_i. To explain the behaviors of the curves, for

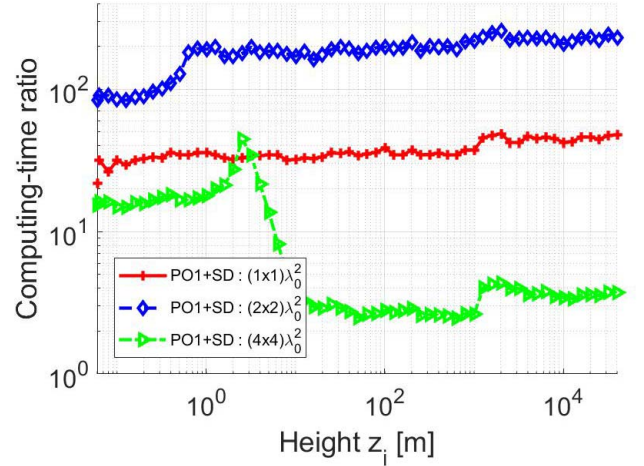Fig. 5. Computing time ratio t^{PO1}/t^{PO1+SD} versus z_i. $l'_x = l'_y = (1, 2, 4)\lambda_0$. The parameters are the same as in Fig. 4.
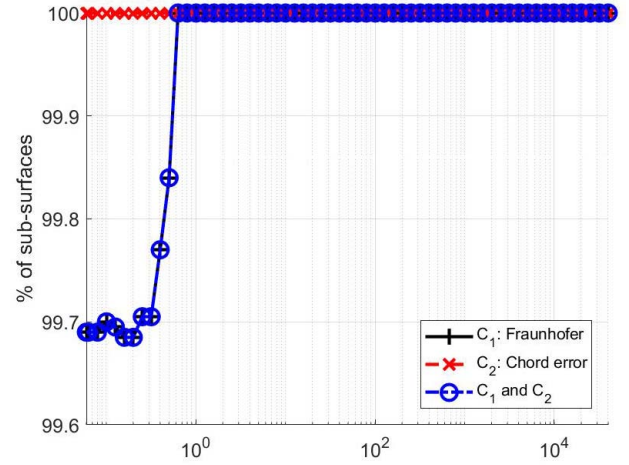

Fig. 6. Percentages of the subsurfaces, which satisfy the Fraunhofer [C_1, (13)], the chord error [C_2, (20)], and (C_1 and C_2) criteria, versus z_i. $(l_x, l_y) = (2, 2)\lambda_0$.

$l'_x = l'_y = 2\lambda_0$, Fig. 6 plots the percentages of the subsurfaces $\{p_{C_1}, p_{C_2}, p_{C_{1,2}}\}$, which satisfies the Fraunhofer (C_1, (13)) and the chord error (C_2, (20)) criteria versus z_i. Fig. 7 plots the same variations as in Fig. 6 but for $l'_x = l'_y = 4\lambda_0$ and the y scale differs. As we can see in Fig. 5, for $l'_x = l'_y = \{1, 2\}\lambda_0$, the time saving increases with z_i since the Fraunhofer C_1 criterion, p_{C_1}, increases as z_i increases, whereas the chord error C_2 criterion is always satisfied ($p_{C_2} = 100\%$ $\forall z_i$). The same remark holds for $l'_x = l'_y = 1\lambda_0$ (not shown).

In addition, for small z_i and $l'_x = l'_y = 4\lambda_0$, the agreement in Fig. 4 is better because most contributions of the subsurfaces are calculated without acceleration (comparison of Fig. 6 with Fig. 7, where $p_{C_{1,2}} = \{99.7, 95\}\%$ for z_i near zero, respectively).

The computing time ratio t^{PO1}/t^{PO1+SD} is directly related to the complexity. From (25), it is expressed as $1/\eta^{PO1+SD}$. For all the N subsurfaces, if the two criteria are satisfied, then the time ratio is $M_x M_y/N$. For $l'_x = l'_y = (1, 2)\lambda_0$, we obtain $\{4001^2/400^2, 4001^2/200^2\} \approx \{100, 400\}$. From Fig. 5, the asymptotic values are nearly these values divided by 2.
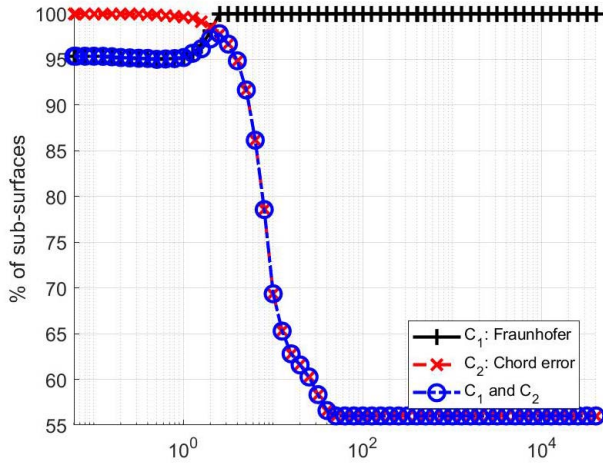
Fig. 7.   Same variations as shown in Fig. 6 but for $l'_x = l'_y = 4\lambda_0$, and the y-scale differs.

Fig. 5 also shows that the choice of the lengths (l'_x, l'_y) must be optimized with respect to r_i but cannot exceed an upper limit obtained from the chord error criterion (20). Typically, for a plane surface and for $r_i \rightarrow \infty$, the numbers (N, l'_x, l'_y) tend to $(1, L_x, L_y)$, but if the surface is strongly curved, these asymptotic values cannot be reached.

Indeed, for $l'_x = l'_y = 4\lambda_0$, Fig. 5 shows that the time saving increases and next decreases. This behavior is directly related to Fig. 7. For z_i close to 0, the criterion C_1 is not fully satisfied $p_{C_1} \approx 95\%$, whereas the criterion C_2 is fully satisfied $p_{C_2} \approx 100\%$. As z_i increases, p_{C_1} increases to tend toward 100%, whereas p_{C_2} decreases and then $p_{C_{1,2}}$ decreases to tend toward 55%. Then, there is an antagonist behavior between C_1 and C_2, which produces an optimized value, for which the method is the most efficient.

From (20), for $r_i \rightarrow \infty$, $r_{iz} \rightarrow 1$, the criterion is then satisfied for the monostatic case if $d = d_{\max} = \sqrt{\lambda_0/(2n_0) \max(\gamma'_{xx}/2 + \gamma'_{yy}/2 + \gamma'_{xy})} \approx 3.559\lambda_0$. This value is consistent with Fig. 5.

At the top of Fig. 8, the percentages of the subsurfaces, which satisfy the Fraunhofer (C_1, (13)) and the chord error (C_2, (20)) criteria, are plotted versus z_i. In addition, in the legend, the label "C_{10}" means that in (13) $\sin \phi'_i = \sin \phi'_s = 1$, which corresponds to the conventional Fraunhofer criterion. At the bottom, the corresponding computing time ratio t^{PO1}/t^{PO1+SD} is plotted versus z_i.

If the conventional criterion C_{10} is applied instead of C_1, then for small values of z_i, the percentage of subsurfaces satisfying C_{10} is smaller than that satisfying C_1 because C_{10} is an upper limit of C_1. Then, the resulting computing time is approximately multiplied by two.

B. Double Bounce

In this section, the monostatic SC ρ of the DB is computed from PO2.

1) Case a = 0: To produce a DB, a dihedral composed of two connected rectangular plates of the same lengths (L_x, L_y) and shown in Fig. 9 is considered. Scatterer 1 is defined by $y < 0$ and scatterer 2 by $y \geq 0$. The lengths with respect to
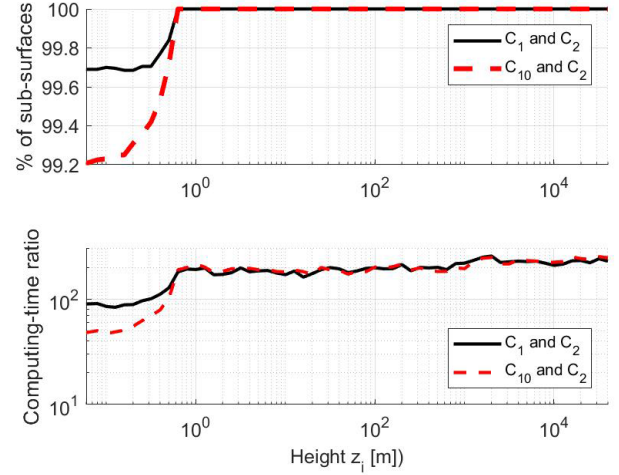

Fig. 8.   Percentages of the subsurfaces, which satisfied the Fraunhofer [C_1, (13)] and the chord error [C_2, (20)] criteria, versus z_i. $(l_x, l_y) = (2, 2)\lambda_0$ (top). Corresponding computing time ratio t^{PO1}/t^{PO1+SD} versus z_i (bottom).
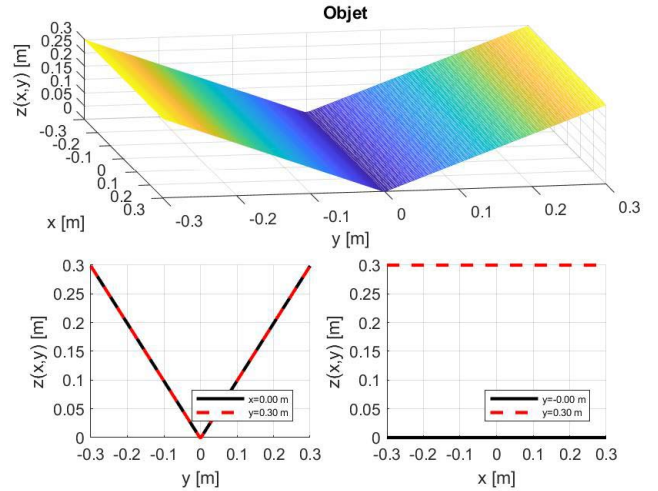

Fig. 9.   Geometry for the computation of the monostatic SC of the DB. Scatterer 1 is defined by $y < 0$ and Scatterer 2 by $y \geq 0$.

the x- and y-directions are $L_x = 20\lambda_0$ and $L_y = 10\sqrt{2}\lambda_0$, respectively, in which $\lambda_0 = 3$ cm (the radar frequency is $f = 10$ GHz). The angles between the y-direction and the plates are $\pi/4 + \pi/2$ and $\pi/4$, respectively. The sampling step with respect to the x- and y-directions is $\Delta x = \Delta y = \lambda_0/10$ and $(M_{x,1}, M_{y,1}, M_{x,2}, M_{y,2}) = (201, 101, 201, 101)$. In addition, the positions of the receiver/transmitter are $x_i = y_i = 0$ and z_i ranges from 0.1 to 100 m $> 4 \max(2L_y \cos(\pi/4), L_x)^2/\lambda_0 = 48$ m, which is the conventional Fraunhofer distance.

At the top, Fig. 10 plots the square modulus (RCS) of the monostatic SC, ρ, versus z_i. In addition, at the bottom, to better see the differences, the ratio $|\rho^{PO2+SD}/\rho^{PO2}|^2$ is plotted in dB scale (becoming a difference). In the legend, the labels:

1) "PO2" means that the SC is computed from (10);
2) "PO2+SD ($l'_{x,1} \times l'_{y,1}$)" ($l'_{x,1} = l'_{x,2}, l'_{y,1} = l'_{y,2}$) means that the SC is computed from (9) and (22) and $n_0 = 10$;
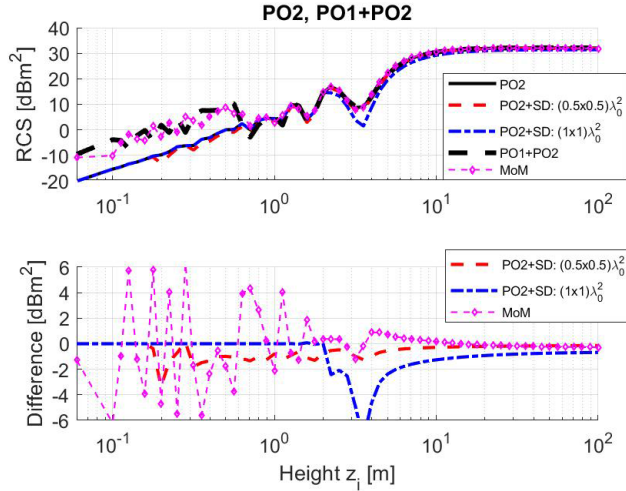3) "PO1+PO2" means that the SC is computed from (9) and (10);

Fig. 10. Square modulus $|\rho|^2$ in dBm^2 scale of the monostatic SC computed from PO2 and PO1+PO2 (without acceleration) versus z_i (top). Difference in dB scale $|\rho^{PO2+SD}|^2$ (dB)$-|\rho^{PO2}|^2$ (dB) (against PO2 without acceleration) (bottom). $l'_{x,1} = l'_{y,1} = l'_{x,2} = l'_{y,2} = \{0.5, 1\}\lambda_0$ and $n_0 = 10$.

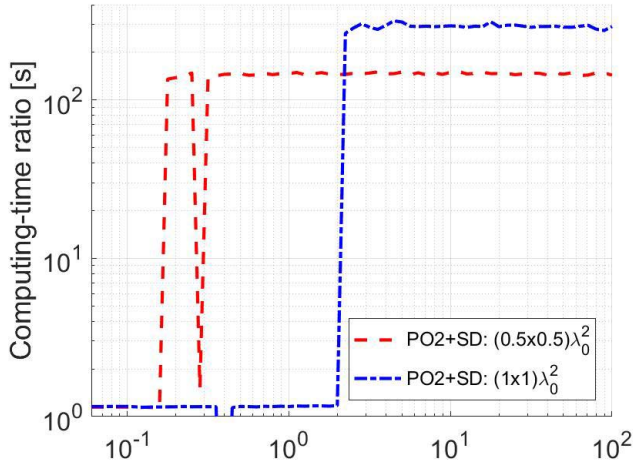Fig. 11. Computing time ratio t^{PO2}/t^{PO2+SD} versus z_i.

4) "MoM" means that the SC is computed from the full-wave method of moments, for which the sampling step is $\lambda_0/8$.

The subsurface lengths are $l'_{x,1} = l'_{y,1} = l'_{x,2} = l'_{y,2} = \{0.5, 1\}\lambda_0$ and are constant according to z_i. In addition, the numbers of the subsurfaces samples of scatterers $i = \{1, 2\}$ are $M_{x,p_i} = M_{y,p_i} = \{5, 10\} \forall (p, i)$ and the numbers of the subsurfaces of scatterers 1 and 2 are $P_1 = P_2 = \{800, 200\}$.

For small values of z_i, Fig. 10 shows a good agreement between PO2 and PO2+SD because, as shown in Fig. 11 [and also Fig. 12 for $(l'_{x,p}, l'_{y,p}) = (0.5, 0.5)\lambda_0$ $(p = \{1, 2\})$], most of the subsurface pair contributions are computed without acceleration. Next, as z_i increases, the difference increases and in the Fraunhofer region, the opposite effect occurs and the difference does not exceed 0.5 dB.

Fig. 10 also reveals that for small values of z_i, the main contribution is given from PO1, whereas the opposite effect occurs for large values of z_i. In addition, a satisfactory agreement is obtained between the MoM and "PO1 + PO2" results, especially in the far field. In the near field, the difference can
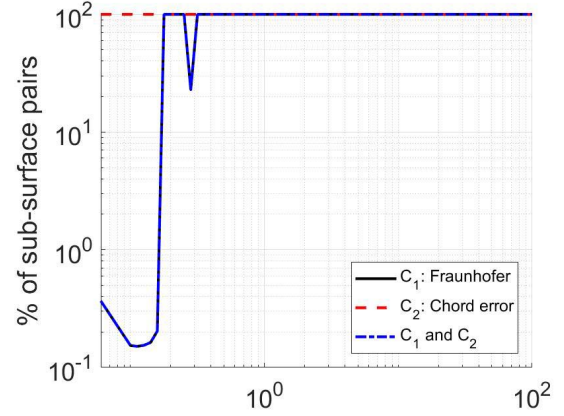

Fig. 12. Percentage $\{p_{C_1}, p_{C_2}, p_{C_{1,2}}\}$ of the pairs of the subsurfaces (between scatterers 1 and 2), which satisfy the Fraunhofer [C_1, (28)], the chord error [C_2, (29)], and (C_1 and C_2) criteria, versus z_i. $(l'_{x,p}, l'_{y,p}) = (0.5, 0.5)\lambda_0$ $(p = \{1, 2\})$.

be attributed to the fact that PO does not account for the edge diffraction.

Fig. 11 plots the computing time ratio t^{PO2}/t^{PO2+SD} versus z_i. As expected, the time saving is significant for the highest values of z_i and it is larger for $l'_{x,1} = l'_{y,1} = l'_{x,2} = l'_{y,2} = l'_x = \lambda_0$, but the range over z_i is larger for $l'_x = 0.5\lambda_0$.

Like PO1, to give an explanation, Fig. 12 plots the percentages $\{p_{C_1}, p_{C_2}, p_{C_{1,2}}\}$ of the pairs of subsurfaces (between scatterers 1 and 2), which satisfy the Fraunhofer [C_1, (28)], the chord error [C_2, (29)], and (C_1 and C_2) criteria, versus z_i. As expected, for $a = 0$, the chord error criterion is satisfied for any z_i ($p_{C_2} = 100\%$), whereas p_{C_1} differs from 100% for $z_i = 0$, next decreases (it is not a monotonic function of z_i), and tends toward 100% for large values of z_i. For $l'_x = \lambda_0$, simulations not reported here showed that $p_{C_{1,2}}$ has the same behavior as that computed for $l'_x = 0.5\lambda_0$ with the main difference that the time saving is significant for a larger value of z_i. This explains the behaviors in Fig. 11.

The computing time ratio t^{PO2}/t^{PO2+SD} is directly related to the complexity. From (35), it is expressed as $1/\eta^{PO2+SD}$. For all the $N = N_1 N_2$ subsurfaces, if the two criteria are satisfied, then the time ratio is $M_{x,1}M_{y,1}M_{x,2}M_{y,2}/N$. For $l'_x = (0.5, 1)\lambda_0$, we obtain $\{(201 \times 101)^2/640\,000, (201 \times 101)^2/40\,000\} \approx 10^4 \times \{0.64, 10.3\}$. From Fig. 11, we obtain $\{143, 290\}$, which is 4.5 and 35.5 times smaller than the theoretical time savings. This difference can be attributed by the fact that the codes are written in MATLAB (not optimized for the loops) and that many additional tests and auxiliary variables are introduced for SD + PO2 method.

2) Case $a \neq 0$: Fig. 13 plots the same geometry as in Fig. 9 but $a = 0.5\lambda_0$ and the periods $\Lambda_x = L_x$ and $\Lambda_y = L_y/2$. Fig. 14 plots the same variations as in Fig. 10 but the object is defined from Fig. 13 ($a \neq 0$). Fig. 15 plots the corresponding computing time ratio t^{PO2}/t^{PO2+SD} versus z_i. Fig. 16 plots the same variations as in Fig. 12, but the object is defined from Fig. 13 ($a \neq 0$).

The comparison of Fig. 14 with Fig. 10 shows that the RCS computed from PO1+PO2 strongly differs and the difference slightly increases in comparison with $a = 0$. Since $a \neq 0$, the percentage of the subsurface pairs p_{C_2} associated with the
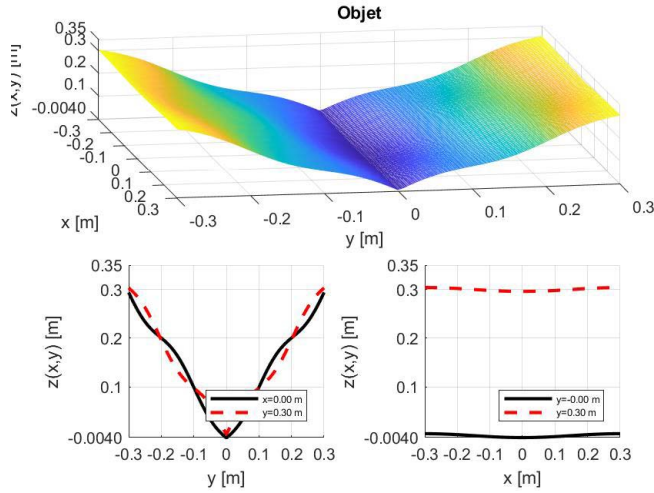
Fig. 13. Same geometry as shown in Fig. 9 but $a = 0.5\lambda_0$ and the periods $\Lambda_x = L_x$ and $\Lambda_y = L_y/2$.
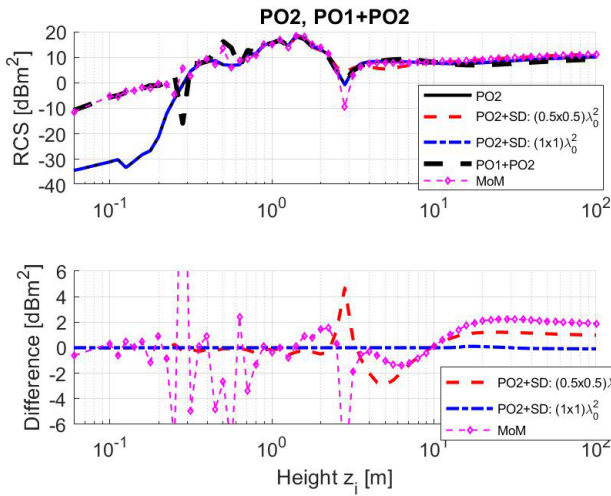

Fig. 15. Computing time ratio t^{PO2}/t^{PO2+SD} versus z_i. The object is defined from Fig. 13 ($a \neq 0$).

Fig. 14. Same variations as shown in Fig. 10 but the object is defined from Fig. 13 ($a \neq 0$).

Fig. 16. Same variations as shown in Fig. 12 but the object is defined from Fig. 13 ($a \neq 0$) and $(l'_{x,p}, l'_{y,p}) = (1, 1)\lambda_0$ ($p = \{1, 2\}$).

chord error criterion C_2 can differ from 100%. For $l'_x = 0.5\lambda_0$, simulations not reported here, showed that $p_{C_{1,2}}$ is nearly the same as that plotted in Fig. 12 and that $p_{C_2} = 100\%$ for any z_i. This explains why the time saving is nearly the same in Figs. 11 and 15.

For $l'_x = \lambda_0$, Fig. 16 shows that $\{p_{C_1}, p_{C_2}, p_{C_{1,2}}\}$ strongly differ from those plotted in Fig. 12. First, p_{C_2} has a similar behavior as that obtained from PO1 and depicted in Fig. 7: it is a decreasing function of z_i. In addition, since $a \neq 0$, for small values of z_i, p_{C_2} is smaller than 100%, unlike in Fig. 12. Second, p_{C_1} is not a monotonic function and does not tend toward 100% because subsurface pairs are in the near field independently of z_i. The resulting percentage $p_{C_{1,2}} \leq (p_{C_1}, p_{C_2})$ (by definition) and since $p_{C_{1,2}} \neq p_{C_1}$ or $p_{C_{1,2}} \neq p_{C_2}$, the subsurface pairs that satisfy criteria C_1 and C_2 are not the same. Indeed, C_1 and C_2 are independent. In the far field, from Fig. 16, a percentage of $p_{C_{1,2}} \approx 1\%$ is not enough to have a significant time saving ($t^{PO2}/t^{PO2+SD} \approx 1.16$ instead of 147 for $l'_x = 0.5\lambda_0$) in Fig. 15.
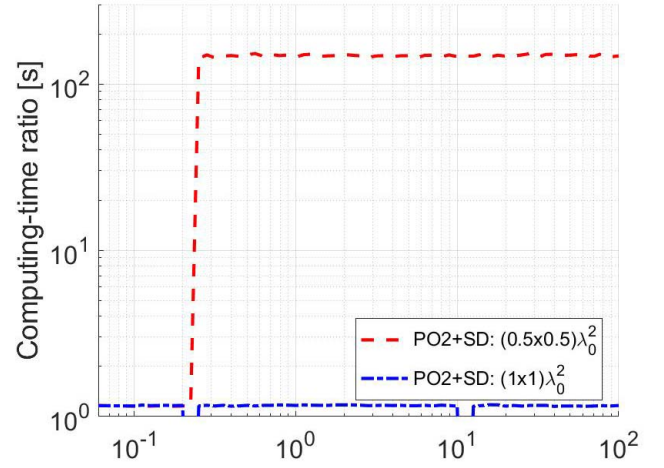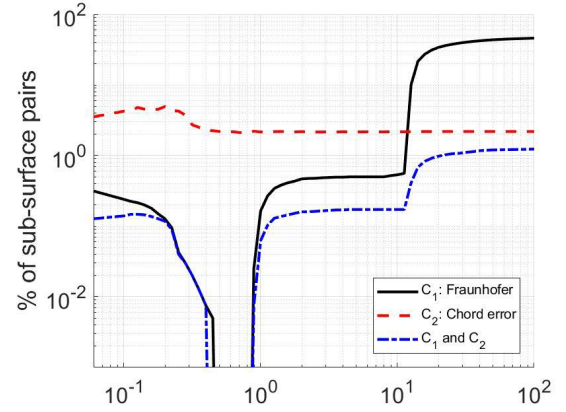
V. CONCLUSION

To accelerate the computation of the SB and DB contributions of PO backscattering (in the near and far fields), the SD is developed. It is based on two physical criteria, the Fraunhofer and chord criteria, for which their derivations are generalized in this paper. For the computation of the SB contribution, the resulting algorithm PO1+SD provides significant time savings in comparison with the direct computation of the double integral. For the computation of the DB contribution, PO2+SD method is also very efficient in terms of time saving especially in the far field, for which the computing time can be reduced by a factor ranging from 100 to 300 in comparison with the conventional quadruple numerical integrations.

For objects with more complex shapes, e.g., object with self-shadowing, the visible function can be computed from ray-based techniques or similar algorithms. For any scattering problem solved from the PO, it is important to underline that the computation of the visible function is inherent to the problem whatever the method used to accelerate the PO. In addition, recently, Thomet et al. [29] showed that the shadowing effect can be modeled by using the PO shadow

radiation. This avoids to calculate the visible function from ray-tracing-based algorithms which can be time consuming.

The SD algorithm is highly parallelizable and can be further accelerated if it is implemented on multi-cores or GPU architectures. For PO1, all the integrals of the subsurfaces can be independently evaluated and then can be parallelized. The RAM requirement depends on the choice of the integration technique. From a simple trapezoidal rule, this requirement is near zero. For PO2, all the integrals between the subsurfaces of scatterers 1 and 2 can also be independently evaluated and they can be parallelized. From a simple trapezoidal rule, this memory requirement is near zero. To sum up, only the fields on the subsurfaces must be stored and for a parallelized version of the code, the memory requirement is proportional to the number of subsurfaces.

The most restrictive criterion (chord error) is related to the curvature of the surface. To overcome this issue, the prospect of this paper is to incorporate the spherical structure up to the second order [in (12), the term in δ^2 would be kept] of the incident wave into the calculation of the surface integral. Then, as shown in [5], in (23) and (34), the sinc function is changed by the modified Fresnel integrals, but simplifying assumptions must be introduced. Another means is to extend the algorithm to multi levels, which consists in dividing subsurfaces into subsubsurfaces of smaller areas, for which the two criteria become valid.

REFERENCES

[1] R. F. Harrington, *Field Computation By Moment Methods*. Hoboken, NJ, USA: Wiley, 2000.

[2] R. Bhalla, H. Ling, J. Moore, D. J. Andersh, S. W. Lee, and J. Hughes, "3D scattering center representation of complex targets using the shooting and bouncing ray technique: A review," *IEEE Antennas Propag. Mag.*, vol. 40, no. 5, pp. 30–39, Oct. 1998.

[3] P. Pouliguen, R. Hemon, C. Bourlier, J. F. Damiens, and J. Saillard, "Analytical formulae for radar cross section of flat plates in near field and normal incidence," *Prog. Electromagn. Res.*, vol. 9, pp. 263–279, 2008.

[4] A. Vallecchi, "Physical optics curved-boundary dielectric plate scattering formulas for an accurate and efficient electromagnetic characterization of a class of natural targets," *IEEE Trans. Geosci. Remote Sens.*, vol. 46, no. 6, pp. 1657–1666, Jun. 2008.

[5] C. Bourlier and P. Pouliguen, "Useful analytical formulae for near-field monostatic radar cross section under the physical optics: Far-field criterion," *IEEE Trans. Antennas Propag.*, vol. 57, no. 1, pp. 205–214, Jan. 2009.

[6] C. Corbel, C. Bourlier, N. Pinel, and J. Chauveau, "Rough surface RCS measurements and simulations using the physical optics approximation," *IEEE Trans. Antennas Propag.*, vol. 61, no. 10, pp. 5155–5165, Oct. 2013.

[7] G. Kubické, C. Bourlier, M. Delahaye, C. Corbel, N. Pinel, and P. Pouliguen, "Bridging the gap between the Babinet principle and the physical optics approximation: Vectorial problem," *Radio Sci.*, vol. 48, no. 5, pp. 573–581, Sep. 2013.

[8] S. Karaca and A. A. Ergin, "Closed-form time domain PO expressions of the electric field scattered from PEC objects illuminated by an electric dipole," *IEEE Trans. Antennas Propag.*, vol. 63, no. 10, pp. 4477–4485, Oct. 2015.

[9] A. Ludwig, "Computation of radiation patterns involving numerical double integration," *IEEE Trans. Antennas Propag.*, vol. 16, no. 6, pp. 767–769, Nov. 1968.

[10] P. Pouliguen, P. Gadenne, and J. Y. Marty, "Radar reflectivity of a target illuminated by a spherical wave," in *Proc. AGARD*, Oct. 1996, pp. 7–10.

[11] A. Boag, "A fast physical optics (FPO) algorithm for high frequency scattering," *IEEE Trans. Antennas Propag.*, vol. 52, no. 1, pp. 197–204, Jan. 2004.

[12] J. Zhang, W. M. Yu, X. Y. Zhou, and T. J. Cui, "Efficient evaluation of the physical-optics integrals for conducting surfaces using the uniform stationary phase method," *IEEE Trans. Antennas Propag.*, vol. 60, no. 5, pp. 2398–2408, May 2012.

[13] L. Corucci, E. Giusti, M. Martorella, and F. Berizzi, "Near field physical optics modelling for concealed weapon detection," *IEEE Trans. Antennas Propag.*, vol. 60, no. 12, pp. 6052–6057, Dec. 2012.

[14] Y. An, D. Wang, and R. Chen, "Improved multilevel physical optics algorithm for fast computation of monostatic radar cross section," *IET Microw., Antennas Propag.*, vol. 8, no. 2, pp. 93–98, Jan. 2014.

[15] J. Zhang, B. Xu, and T. J. Cui, "An alternative treatment of saddle stationary phase points in physical optics for smooth surfaces," *IEEE Trans. Antennas Propag.*, vol. 62, no. 2, pp. 986–991, Feb. 2014.

[16] M. Roudstein, Y. Brick, and A. Boag, "Multilevel physical optics algorithm for near-field double-bounce scattering," *IEEE Trans. Antennas Propag.*, vol. 63, no. 11, pp. 5015–5025, Nov. 2015.

[17] F. S. D. Adana, S. Nieves, E. Garcia, I. Gonzalez, O. Gutierrez, and M. F. Catedra, "Calculation of the RCS from the double reflection between planar facets and curved surfaces," *IEEE Trans. Antennas Propag.*, vol. 51, no. 9, pp. 2509–2512, Sep. 2003.

[18] M. F. Catedra, C. Delgado, S. Luceri, O. G. Blanco, and F. S. de Adana, "Physical optics analysis of multiple interactions in large scatters using current modes," *IEEE Trans. Antennas Propag.*, vol. 54, no. 3, pp. 985–994, Mar. 2006.

[19] C. Delgado, J. M. Gomez, and F. Catedra, "Analytical field calculation involving current modes and quadratic phase expressions," *IEEE Trans. Antennas Propag.*, vol. 55, no. 1, pp. 233–240, Jan. 2007.

[20] G. Kubicke, C. Bourlier, and J. Saillard, "Polarimetric bistatic signature of a faceted octahedron in high-frequency domain," *Prog. Electromagn. Res.*, vol. 71, pp. 173–209, Oct. 2007.

[21] G. Kubicke, C. Bourlier, and J. Saillard, "High-frequency bistatic scattering by depolarizing, nearly omnidirectional reflectors: Higher order polyhedral reflectors," *IEEE Trans. Antennas Propag.*, vol. 56, no. 9, pp. 3029–3035, Sep. 2008.

[22] J. A. Jackson, "Analytic physical optics solution for bistatic, 3D scattering from a dihedral corner reflector," *IEEE Trans. Antennas Propag.*, vol. 60, no. 3, pp. 1486–1495, Mar. 2012.

[23] F. Obelleiro-Basteiro, J. Luis Rodriguez, and R. J. Burkholder, "An iterative physical optics approach for analyzing the electromagnetic scattering by large open-ended cavities," *IEEE Trans. Antennas Propag.*, vol. 43, no. 4, pp. 356–361, Apr. 1995.

[24] F. Obelleiro, J. Campos-Nino, J. L. Rodriguez, and A. G. Pino, "A segmented approach for computing the electromagnetic scattering of large and deep cavities," *Prog. Electromagn. Res.*, vol. 19, pp. 129–145, 1998.

[25] A. Boag, "A fast iterative physical optics (FIPO) algorithm based on non-uniform polar grid interpolation," *Microw. Opt. Technol. Lett.*, vol. 35, no. 3, pp. 240–244, Nov. 2002.

[26] R. J. Burkholder, C. Tokgoz, C. J. Reddy, and W. O. Coburn, "Iterative Physical Optics for radar scattering predictions," *J.-Appl. Comput. Electromagn. Soc.*, vol. 24, no. 2, pp. 241–258, Apr. 2009.

[27] A. Thomet, G. Kubické, C. Bourlier, and P. Pouliguen, "Optimizing Iterative Physical Optics by using an ACA compression on interaction matrices," in *Proc. IEEE Int. Symp. Antennas Propag. USNC/URSI Nat. Radio Sci. Meeting*, Jul. 2015, pp. 1498–1499.

[28] A. Thomet, G. Kubické, C. Bourlier, and P. Pouliguen, "Low computational cost method for scattering of large cavities based on ACA compression of Iterative Physical Optics," in *Proc. Int. Conf. Electromagn. Adv. Appl. (ICEAA)*, Sep. 2015, pp. 207–210.

[29] A. Thomet, G. Kubické, C. Bourlier, and P. Pouliguen, "Improvement of Iterative Physical Optics using the physical optics shadow radiation," *Prog. Electromagn. Res.*, vol. 38, pp. 1–13, 2014.

[30] W. Gordon, "Far-field approximations to the Kirchoff-Helmholtz representations of scattered fields," *IEEE Trans. Antennas Propag.*, vol. AP-23, no. 4, pp. 590–592, Jul. 1975.